

Invited Article

Spectral characteristics of “mixed” sesquioxide $\text{Yb}:(\text{Gd},\text{Lu})_2\text{O}_3$ transparent ceramics

Mykhailo Chaika ^a, Stanislav Balabanov ^{b,*}, Dmitry Permin ^b^a Institute of Low Temperature and Structure Research Polish Academy of Science, ul. Okolna 2, 50-422, Wroclaw, Poland^b G.G. Devyatikh Institute of Chemistry of High-Purity Substances, Russian Academy of Sciences, Tropinin Str. 49, 603951, Nizhny Novgorod, Russia

ARTICLE INFO

Keywords:
 $\text{Yb}:(\text{Gd},\text{Lu})_2\text{O}_3$
 Spectroscopic properties
 Near-infrared
 High-powerful lasers
 Yb-doped sesquioxides

ABSTRACT

In this work, Yb^{3+} -doped $\text{Gd}_{1.4}\text{Lu}_{0.5}\text{Yb}_{0.1}\text{O}_3$ optical quality ceramics were successfully fabricated for the first time, to the best of our knowledge. The absorption and emission spectra were measured, spectroscopic investigations of 1-μm emission were carried out, and optical gain properties were analysed. The stimulated-emission cross-sections were $9.7 \cdot 10^{-21} \text{ cm}^2$ and $3.7 \cdot 10^{-21} \text{ cm}^2$ (calculated using the Fuchtbauer-Ladenburg equation) at 1031 nm and 1073 nm respectively. The calculated values were close to the estimated value of emission cross-sections for other Yb-doped sesquioxides. All the results show that $\text{Yb}:(\text{Gd},\text{Lu})_2\text{O}_3$ ceramics can be used as a potential active medium for mid-infrared high-power lasers.

1. Introduction

Due to the good thermal and mechanical properties, Yb^{3+} -doped ceramic laser materials have attracted a great deal of attention in the recent decades [1,2]. For commercial high-power continuous and mode-locking laser systems operating in the 1-μm-range, Yb^{3+} -based laser materials have the potential to substitute those based on Nd^{3+} [3, 4]. However, a disadvantage of Yb^{3+} laser systems is the operation in a quasi-three- or quasi-four-level scheme at room temperature, as the lower laser level belongs to the ground state manifold ${}^2\text{F}_{7/2}$ and is considerably thermally populated [5]. This leads to reabsorption of the emitted laser light and, therefore, to higher lasing thresholds and reduced efficiency.

The spectroscopic properties of the Yb^{3+} -doped host strongly depend on the properties of the matrix; therefore, this determines the laser performance of these materials. The main feature of Yb^{3+} ions compared to other rare earth ions is a strong interaction of the Yb^{3+} electronic states with the crystal lattice which leads to homogeneous broadening of the transition lines and to vibronic features [6]. For example, the glasses and disordered crystals or ceramics are characterised by multiple Yb^{3+} sites leading to inhomogeneous broadening of absorption and emission spectra. Therefore, the shapes of the optical spectra and the values of the absorption and emission cross-sections vary significantly [4].

Due to its unique properties, the proposed new host for Yb^{3+} -based lasers can enhance the advantages of Yb^{3+} ions and eliminate the

disadvantages. Despite the numerous papers published in the last few decades, the potential of the Yb^{3+} -doped laser materials is currently limited by the lack of knowledge of the spectroscopic properties of these new Yb^{3+} -doped laser materials [7]. Consequently, studying the spectroscopic properties of the new Yb^{3+} -doped laser matrix is an urgent task.

Yb^{3+} -doped laser materials can be prepared in the form of single crystals [8] by melting or solution methods, in the form of glasses, and as ceramics by consolidation of nanopowders [5,9]. Transparent ceramics have become increasingly important for applications in which materials with good optical properties and high mechanical and thermal stress resistance are required [3,10–13]. Various host materials for laser ceramics have been progressively investigated [5,10,14]. Yb-doped sesquioxides are the potential alternatives to Yb:YAG for power scaling because of their desirable thermal properties. The thermal conductivity of undoped Y_2O_3 ceramics is as high as 12.8 W/m·K at 300 K [15]. However, the strong electron-phonon interaction causes characteristic spectral broadening, especially in the case of Y_2O_3 with moderate values of cross sections [14].

The rapid development of ceramic technology makes it possible to synthesize RE_2O_3 transparent ceramics based on Sc_2O_3 , Y_2O_3 , and Lu_2O_3 matrices [3,8,10,11,14,15]. Despite this progress, there are no published works on the study of Gd_2O_3 -based laser ceramics. The main reason for this is the phase transition of cubic Gd_2O_3 to the monoclinic phase at temperatures as low as 1200 °C. The phase transition provokes

* Corresponding author.

E-mail address: balabanov@ihps-nnov.ru (S. Balabanov).

accelerated grain growth, which leads to pore entrapment, and the change in lattice volume causes the sample to crack. The possible solution to this problem is to enlarge the phase transition temperature by the addition of cubic oxides with a higher temperature C→B transition such as Lu_2O_3 and/or Yb_2O_3 and/or to decrease the sintering temperature.

In this work, Yb^{3+} -doped $\text{Gd}_{1.4}\text{Lu}_{0.5}\text{Yb}_{0.1}\text{O}_3$ ceramics were successfully obtained for the first time, to the best of our knowledge. At a Gd_2O_3 content in the matrix of 70% mol. ceramics have a relatively high optical quality. The absorption and emission spectra were measured, the spectroscopic investigations of 1- μm emission were carried out, and the optical gain properties were analysed.

2. Experimental

Synthesis of powders and hot pressing of ceramics was done similarly to that described in Ref. [16]. Briefly, the initial oxides of ytterbium, gadolinium, and lutetium were dissolved in an aqueous solution of nitric acid. A sintering additive lithium fluoride (1 wt%) and an aminoacetic acid in a molar fraction of 1:1.2 with respect to nitrate groups was added to the solution. After drying, the precursor was heated in a muffle furnace and self-propagating high-temperature synthesis began at about 300 °C. As a result of the combustion reaction, $\text{LiF:Gd}_{1.4}\text{Lu}_{0.5}\text{Yb}_{0.1}\text{O}_3$ nanopowders (1 wt%) were obtained. After additional calcination in air at 750 °C for 0.5 h, the powders were pre-compacted in a steel mould with a pressure of ~10 MPa, and then placed in a graphite mould, 13 mm in diameter. Hot pressing ($P = 50$ MPa) was performed using home-made equipment at a maximum temperature of 1550 °C for 1 h in a vacuum (~10 Pa). Due to the stresses caused by the phase transition from the cubic to the monoclinic phase during hot pressing, the sample split in half. The ceramics were annealed in air at 1100 °C degrees for 5 h, and then subjected to the standard procedure of grinding and polishing with diamond pastes. The sintering additive was removed during hot pressing and was not contained in the final sample. The thickness of the sample obtained was 1.65 mm. The appearance of the ceramics is shown in Fig. 1.

X-ray diffraction was used to identify the crystallographic structure, unit cell parameters and average particle size. The X'pert PRO PANalytical powder diffractometer with the Cu lamp ($\lambda = 0.154$ nm) was used as an excitation source. The use of a nickel filter provided the monochromatic radiation. All the samples were measured in the range of 10–90°, with 0.026° steps. The composition of the synthesized samples



Fig. 1. Photograph of the $\text{Gd}_{1.4}\text{Lu}_{0.5}\text{Yb}_{0.1}\text{O}_3$ ceramics.

was studied using SEM electron microscopy. The images were recorded by a FEI NOVA NanoSEM 230 high-resolution scanning electron microscope equipped with an EDS spectrometer EDAX Pegasus XM4 (with the Apollo 40 SDD detector), with a primary beam energy of 20 keV. Optimum resolutions (high vacuum) were 1.0 nm and 1.5 nm at 15 kV (TLD-SE) and at 1 kV (TLD-SE), respectively. Beam landing energy was 50 V - 30 kV, and probe current was 0.6 pA–100 nA (continuously adjustable).

Absorbance measurements were made using in-line transmittance and a reflection technique with a Varian Cary 5E UV-VIS-NIR spectrophotometer equipped with an adapter for reflection measurements. Deuterium (200–350 nm) and halogen lamps (350–2500 nm) were used as radiation sources. For detection, a spectrophotometer equipped with a Hamamatsu R928 photomultiplier tube (UV-VIS range) and a cooled PbS detector for the near infrared range were used. The spectrophotometer was equipped with two diffraction gratings – 1200 lines/mm centred on 250 nm for the UV-VIS range and a constant grating with 300 lines/mm centred on 1192 nm for the visible range.

Photoluminescence (emission spectra, luminescence excitation spectra and decay times) was recorded using an Edinburgh Instruments FLS980 spectrofluorimeter equipped with two excitation sources: a continuous xenon lamp with a power of 450 W and a pulse xenon lamp with a power of 150 W. The single and double grating monochromators used in the FLS980 are of the Czerny-Turner configuration with 300 mm (or 2×300 mm) focal length, high optical throughput, excellent stray light rejection, and low temporal dispersion. The excitation monochromator was equipped with a diffraction grating with 1800 lines/mm illuminated at a wavelength of 250 nm, while the emission monochromator was equipped with a diffraction grating with 1800 lines/mm illuminated at a wavelength of 500 nm for the visible range or 1200 nm for the near-infrared range. The spectrofluorimeter was equipped with two detectors – the Hamamatsu R928P photomultiplier for the visible range and the liquid nitrogen cooled Hamamatsu R5509-72 photomultiplier for the infrared range. The fluorescence spectra in the 1 μm region were excited with an InGaAs laser diode (976 nm). In addition, the fluorescence decay curves at 1030 nm were measured at 976 nm excitation using an InGaAs laser diode. All the measurements were taken at room temperature.

3. Results and discussion

3.1. Structure characteristics

Fig. 2 shows the X-Ray diffraction (XRD) of the $\text{Gd}_{1.4}\text{Lu}_{0.5}\text{Yb}_{0.1}\text{O}_3$ transparent ceramics. The XRD results indicated the presence of two phases. The first had a cubic structure similar to those of pure Lu_2O_3 and Gd_2O_3 , and the second had a monoclinic $(\text{Lu},\text{Gd})_2\text{O}_3$ structure. The diffraction data were refined with the cubic $I2_13$ space group for Gd_2O_3 and the $C2/m$ space group for Gd_2O_3 using Rietveld analysis. The structure refinements involved resorting to the FullProfSuite program and using the WinPLOTR, and WinPLOTR-2006 applications. The lattice parameters were: for the cubic phase $a = 10.6864(4)$ Å; for the monoclinic cell $a = 3.413(1)$ Å, $b = 7.229(2)$ Å, $c = 8.957(3)$ Å, $\alpha = 98.66(2)$ °, $\beta = 90^\circ$, $\gamma = 100.76(1)$ °. It should be noted that the reflection peaks of the monoclinic phase were broadened, indicating a lack of completion of the phase transition from the monoclinic to the cubic phase. This fact implies difficulties in the calculations of the monoclinic cell parameters, as well as the weight percentage of these phases.

The presence of the monoclinic phases was expected in the ceramic samples of such a composition. The same results were reported earlier, where the $\text{Gd}_{1.6}\text{Lu}_{0.4}\text{O}_3$ and $\text{Gd}_{1.4}\text{Lu}_{0.6}\text{O}_3$ lutetium gadolinium oxide solid solutions have both monoclinic and cubic phases [17]. The full transformation from the monoclinic to the cubic phase takes place at temperatures higher than 1600 °C for the $(\text{Lu},\text{Gd})_2\text{O}_3$ samples doped by more than 40 at. % Lu; that is higher than in our case. It should be noted that the SEM analysis revealed no secondary phases in our samples

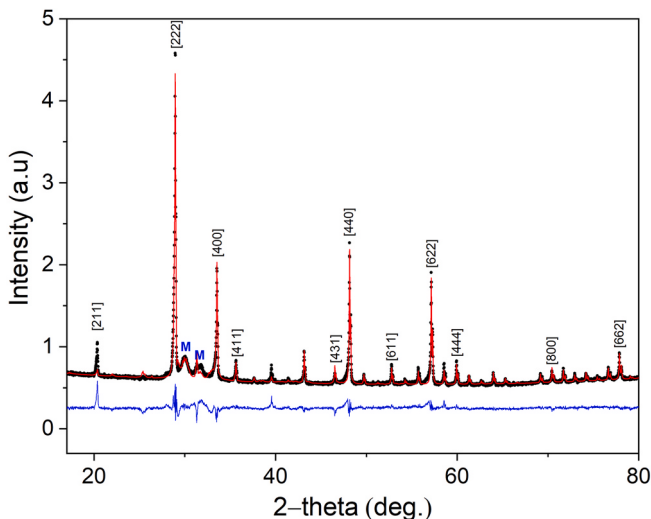


Fig. 2. X-ray diffraction pattern of the $\text{Gd}_{1.4}\text{Lu}_{0.5}\text{Yb}_{0.1}\text{O}_3$ transparent ceramics (black curve), and results of Rietveld refinement analysis (red and blue curve). The M symbol indicates peaks corresponding to monoclinic phase. (For interpretation of the references to colour in this figure legend, the reader is referred to the Web version of this article.)

(Fig. S1). The elemental mapping showed homogeneous distribution of the Gd, Lu, Yb and O elements across the sample (Fig. 3).

3.2. Optical properties

The transmission spectra from 200 nm to 2500 nm of the $\text{Gd}_{1.4}\text{Lu}_{0.5}\text{Yb}_{0.1}\text{O}_3$ ceramic samples are presented in Fig. 4. In-line transmission at 500, 1100, and 2500 nm was 54%, 71%, and 76%, respectively, which is comparable with the other RE_2O_3 ceramics [18, 19]. It should be noted that the transmittance of the mixed $\text{Gd}_{1.4}\text{Lu}_{0.5}\text{Yb}_{0.1}\text{O}_3$ ceramics is comparable with $\text{Yb}^{3+}:\text{Lu}_2\text{O}_3$ transparent ceramics [20–22]. The dotted line shows the calculated in-line transmittance of the defect-free $\text{Gd}_{1.4}\text{Lu}_{0.5}\text{Yb}_{0.1}\text{O}_3$ ceramics. The theoretical transmittance curve was obtained by the Lambert – Beer law:

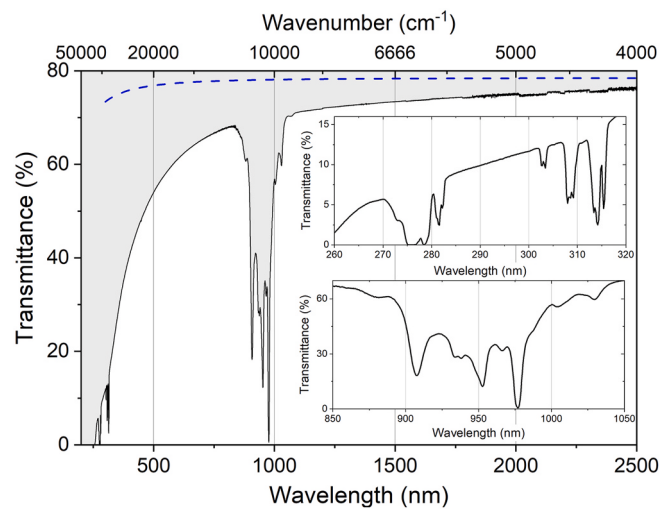


Fig. 4. The transmission spectrum of $\text{Gd}_{1.4}\text{Lu}_{0.5}\text{Yb}_{0.1}\text{O}_3$ ceramics at wavelengths ranging from 200 nm to 2500 nm measured at room temperature. The dotted line presents the theoretical transmission of the defect-free Gd_2O_3 matrix calculated using the refractive index from eq: 2.

$$k = \frac{1}{h} \ln \left[\frac{(1 - R)^2}{T} \right], \quad R = \left[\frac{n_2 - n_1}{n_2 + n_1} \right]^2 \quad (1)$$

where k is the linear optical loss coefficient, h is the ceramic sample thickness, R is the wavelength-dependent reflection coefficient, and T is the linear light transmission coefficient, $T = (1 - R)^2$.

Prediction of the refractive index of the $\text{Gd}_{1.4}\text{Lu}_{0.5}\text{Yb}_{0.1}\text{O}_3$ solid solution at different wavelengths was performed using the Drude (or Silberstein) theory, which was developed to describe the effective refractive index n_{eff} of heterogeneous media in terms of volume fractions [23]:

$$n_{\text{eff}}^2 = (1 - \varphi)n_1^2 + \varphi n_2^2 \quad (2)$$

where n_1 and n_2 are refractive indexes of Gd_2O_3 and Lu_2O_3 phases, respectively, and φ is the volume fraction of the second phase.

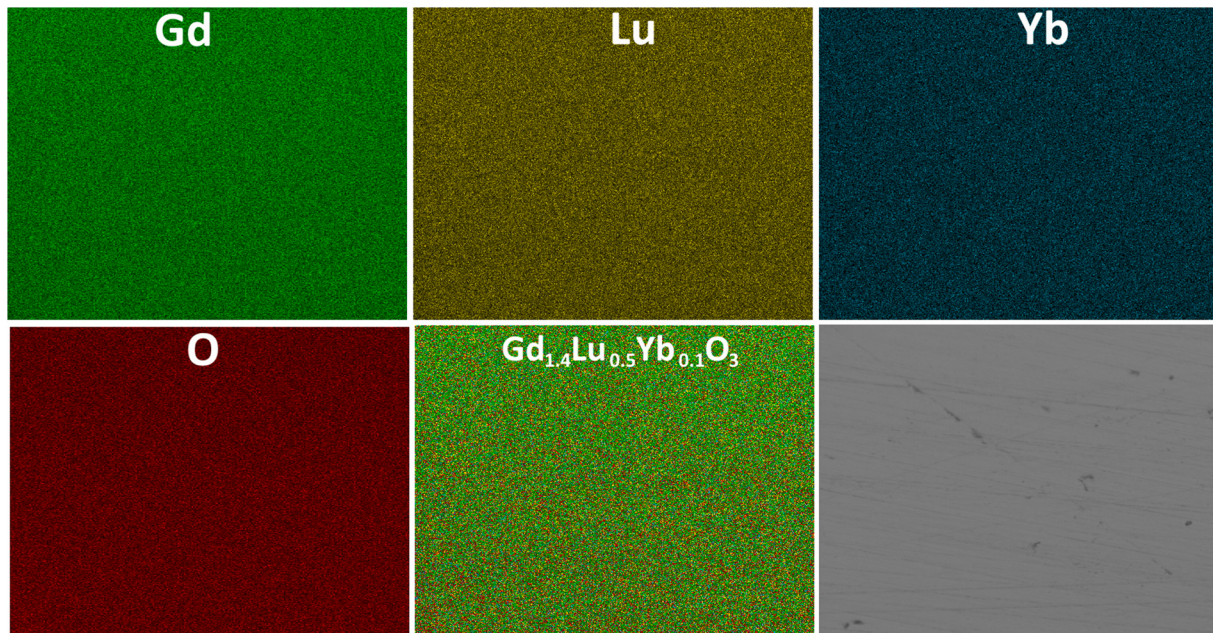


Fig. 3. EDX elemental mapping in $\text{Gd}_{1.4}\text{Lu}_{0.5}\text{Yb}_{0.1}\text{O}_3$ transparent ceramics for Gd, Lu, Yb, and O. The indicated atomic symbols correspond to the EDX.

Due to the low fraction of the Yb_2O_3 phase, the volume fraction of the Yb_2O_3 phase was added to the volume fraction of Lu_2O_3 due to the proximity of its refractive index [24]. Considering the lattice volume of cubic Lu_2O_3 (556 \AA^3) and Gd_2O_3 (640 \AA^3), the volume fractions of Lu_2O_3 and Gd_2O_3 were 27% and 73%, respectively. Refractive indices of cubic Gd_2O_3 and Lu_2O_3 phases obey the Sellmeier equation [24]:

$$\frac{1}{n^2 - 1} = -\frac{A}{\lambda^2} + B \quad (3)$$

where n is the refractive index, and λ is the wavelength, A is the slope of the plot of $(n^2 - 1)^{-1}$ vs. $(\lambda^2)^{-1}$, which gives a measure of the dispersion, and B is the intercept of the plot at $\lambda = \infty$, which gives $n_\infty = (1 + 1/B)^{1/2}$.

The calculated values of A and B are listed in Table 1. However, the refractive indices of the Gd_2O_3 and Lu_2O_3 compounds can be calculated accurately for any wavelength in the visible region.

The absorption bands in the range from 850 to 1050 nm can be ascribed to ${}^2\text{F}_{7/2} \rightarrow {}^2\text{F}_{5/2}$ electronic transitions of Yb^{3+} ions [5]. No Yb^{2+} ions were observed in the sample. The most intense absorption in the range below 240 nm corresponds to interband transitions of the Gd_2O_3 matrix. The lines at 275 nm and 315 nm were attributed to the 4f-4f optical transitions of Gd^{3+} ion from the ground ${}^8\text{S}_{7/2}$ to the excited ${}^6\text{I}_J$ and ${}^6\text{P}_J$ states, respectively. Selective absorption peaks of the host lattice cations indicated that the electron structure of a part of the Gd^{3+} ions in Gd_2O_3 was distorted [25]. We suppose that this distortion was caused by incomplete transformation of the monoclinic to cubic phase in our sample. The absorption cross-section of Yb^{3+} ions was determined according to the following equation:

$$\sigma_{abs} = H/N \quad (4)$$

where σ_{abs} , H and N represent the absorption cross-section, absorption coefficient at a certain wavelength, and concentration of Yb^{3+} ions, respectively.

The cubic $(\text{Lu},\text{Gd})_2\text{O}_3$ phase has the cation density of $2.61 \times 10^{22} \text{ cm}^{-3}$ (32 cations per 1220 \AA^3 unit cell volume with 24 in the C_2 sites and 8 in the C_{3i} sites) and, therefore, concentration of Yb^{3+} ions is $0.13 \times 10^{22} \text{ cm}^{-3}$. The absorption coefficients of Gd^{3+} ions at 275 nm and 315 nm were 48.5 cm^{-1} and 10.5 cm^{-1} , respectively. The absorption spectrum of the sample is shown in Fig. S2. The $\text{Gd}_{1.4}\text{Lu}_{0.5}\text{Yb}_{0.1}\text{O}_3$ cubic phase has two six-coordinated cation sites, with local point group symmetries of C_2 and C_{3i} . According to the literature, Yb^{3+} ions can occupy each site. The C_{3i} contains 25%, and the C_2 site 75% of all Yb ions and both contribute to the total absorption and emission spectra [26]. The absorption lines at 975 nm are caused by the ${}^2\text{F}_{7/2} \leftrightarrow {}^2\text{F}_{5/2}$ electron transitions of Yb^{3+} ions. The absorption coefficient was 28.4 cm^{-1} and the absorption cross-section was $2.18 \cdot 10^{-20} \text{ cm}^2$ (Fig. 6). This agrees with the literature data [3,11].

The laser properties of the Yb^{3+} -doped laser materials are based on the ${}^2\text{F}_{7/2} \leftrightarrow {}^2\text{F}_{5/2}$ electron transitions which caused the appearance of absorption and emission bands in the NIR region. The electron structure of Yb^{3+} is $[\text{Xe}]4f^13$. So, the 4f-shell is almost complete with the exception of one hole, which is responsible for the simple level structure. Two relevant Stark multiplets, ${}^2\text{F}_{5/2}$ and ${}^2\text{F}_{7/2}$ (Fig. 1), are separated by approximately 10000 cm^{-1} ; the next excited configuration is located at $\approx 100,000 \text{ cm}^{-1}$ [4]. In a crystal field of cubic symmetry, the six-fold degenerated $J = 5/2$ manifold is split into a Γ_7 doublet (2') and a Γ_8 quartet (0', 1'), and for octahedral (six-fold) coordination the quartet lies lower. The $J = 7/2$ manifold forms a Γ_8 quartet (1, 2) and two doublets (Γ_6 (0) and Γ_7 (3)).

Table 1
The dispersion parameters [24].

Parameter	Yb_2O_3	Lu_2O_3	Gd_2O_3
$A, 10^{-16} \text{ m}^2$	67.8	65.2	62.0
B	0.3779	0.3839	0.3104

Room-temperature absorption and luminescence spectra corresponding to the intermanifold ${}^2\text{F}_{7/2} \leftrightarrow {}^2\text{F}_{5/2}$ transitions of Yb^{3+} ions in $\text{Gd}_{1.4}\text{Lu}_{0.5}\text{Yb}_{0.1}\text{O}_3$ ceramic are shown in Fig. 5. There is a broad absorption band from 850 nm to 1050 nm, which makes temperature control less critical to ensure stable absorption at 975 nm. The measured luminescence lifetime of the ${}^2\text{F}_{5/2}$ state of Yb^{3+} ions in the $\text{Gd}_{1.4}\text{Lu}_{0.5}\text{Yb}_{0.1}\text{O}_3$ ceramic sample was found to be $1.07(1) \text{ ms}$ (Fig. S3). In the thermal equilibrium, the level populations are Boltzmann-distributed. In the case of pumping and lasing, a considerable part of the active ions is found in the upper manifold. Fast intraband thermalization leads to a separate distribution for each manifold, with most of the excited ions being in (0'). Therefore, laser inversion is only possible here and laser emission will occur from (0') to (1), (2), or (3) leading to intense emission centred at 9922 cm^{-1} (1008 nm), 9712 cm^{-1} (1030 nm), and 9341 cm^{-1} (1072 nm), respectively. It is difficult to realize the necessary high pump intensities and achieve inversion for the (0')-to-(0) (“zero-line”) transition, which is centred at 10244 cm^{-1} (976 nm). Other emission lines contribute to fluorescence. It should be noted that the crystal-field splitting and the assignment of electronic transitions calculation are based on a high resolution low temperature study of a $\text{Yb}: \text{Lu}_2\text{O}_3$ single crystal [26].

At room temperature, Yb has a “quasi-three-level” character; when manifold partition functions are taken into account, at least 5.5% of all Yb^{3+} ions must be pumped into the initial laser Stark level to achieve gain material transparency [27]. In a “quasi-three-level laser scheme” the Yb^{3+} ions are pumped into (0'). “Quasi” refers to the fact that the Stark levels within a multiplet are only “quasi-separate” and are actually connected by a Boltzmann distribution. Lasing occurs most readily for the strong emission transitions at 1030 nm or 1072 nm between the lowest Stark level of the ${}^2\text{F}_{7/2}$ manifold at 10241 cm^{-1} (0') and the Stark levels of the ground manifold at 516 cm^{-1} (2) or 879 cm^{-1} (3).

3.3. Emission cross-sections

Emission cross-section is an important characteristic for predicting the stimulated emission for the laser active media. There are a number of different ways in which emission cross-sections can be determined. The three main possibilities include: 1) the reciprocity method (McCumber method), 2) the Fuchtbauer-Ladenburg (F-L) equation, and 3) direct measurements of small signal or saturated gain [7,28]. Each of these methods introduces a distortion to the calculated value of the emission cross-sections, which must be taken into account. Therefore, the emission cross-section was calculated by two different approaches. First, the

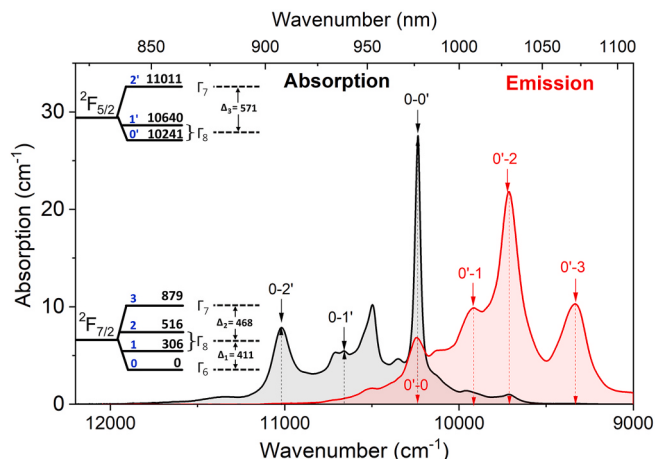


Fig. 5. Room-temperature absorption and emission spectra (${}^2\text{F}_{7/2} \leftrightarrow {}^2\text{F}_{5/2}$ transition) in $\text{Gd}_{1.4}\text{Lu}_{0.5}\text{Yb}_{0.1}\text{O}_3$ ceramics. Inset shows the room-temperature crystal field splitting of ${}^2\text{F}_{5/2}$ and ${}^2\text{F}_{7/2}$ manifolds in $\text{Gd}_{1.4}\text{Lu}_{0.5}\text{Yb}_{0.1}\text{O}_3$ ceramics. Energies of Stark levels are given in cm^{-1} .

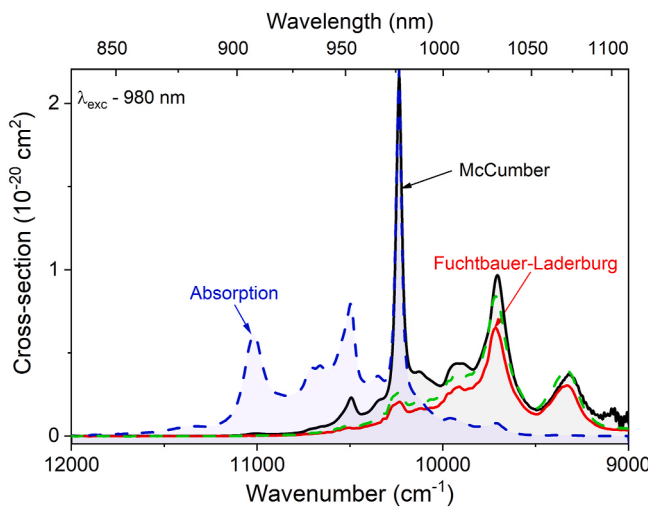


Fig. 6. The absorption (blue dashed line) and emission cross-section spectra calculated by reciprocity method (black solid line), Fuchtbauer-Ladenburg (F-L) equation taking into account the experimental lifetime (red solid line) and the calculated lifetime (green dashed line). (For interpretation of the references to colour in this figure legend, the reader is referred to the Web version of this article.)

Fuchtbauer-Ladenburg equation was used [29]:

$$\sigma_{em}(\lambda) \approx \frac{\lambda^4}{8\pi cn^2\tau_{rad}} \times \frac{\lambda I(\lambda)}{\int \lambda I(\lambda) d\lambda} \quad (6)$$

where $\lambda I(\lambda)/\int \lambda I(\lambda) d\lambda$ is the normalized lineshape function of the experimental emission spectrum $I(\lambda)$, n is the refractive index, c is the speed of light in a vacuum, τ_{rad} is the radiative lifetime, and σ_{em} is the emission cross-section.

The F-L methods use the emission spectral line shapes and the fluorescence lifetime. One of the main problems of this method is related to the measurement errors in the emission spectra and fluorescence lifetime. In order to determine the measured lifetime, the radiative lifetime was estimated from absorption cross-sections. The calculated lifetime is given by $\tau_{cal} = A^{-1}$ where A is the radiative transition rate for Yb^{3+} given by the following equation [30]:

$$A_{rad} = \frac{8\pi cn^2}{\lambda_p^4} \frac{(2J_l + 1)}{(2J_u + 1)} \int \sigma_{abs}(\lambda) d\lambda \quad (7)$$

where λ_p is the wavelength of peak absorption, J_u and J_l are the total momenta for the upper and lower levels and σ_{abs} is the absorption cross-section.

The calculated radiative transition rate was 1208 s^{-1} corresponding to calculated lifetime $\tau_{cal} \sim 0.83 \text{ ms}$. The calculated lifetime corresponds well with that reported in the literature for other Yb-doped sesquioxides (see Table 2). In contrast, the measured lifetime ($\tau_{exp} \sim 1.07 \text{ ms}$) is higher by 23% compared to that calculated [31]. Such difference was caused by the radiative trapping effect [32,33]. The difference in the values of measured and calculated lifetimes is in agreement with the

Table 2
Characteristics of Yb-doped laser materials (the current paper was marked as [C]). The star denotes single crystals.

Host material	C(Yb), at.%	Absorption			Emission			τ (ms)	Thermal Conductivity, (W/m·K)	Ref.
		λ_{abs} (nm)	$\Delta\lambda_{abs}$ (nm)	σ_{abs} (10^{-20} cm^2)	λ_{em} (nm)	$\Delta\lambda_{em}$ (nm)	σ_{em} (10^{-20} cm^2)			
YAG*		941	18	0.82	1030	8.5	2.10	0.95	10.1	[8]
		969	3	0.80						
Y_2O_3^*	5	976	2.5	2.4	1030	12.2	0.98	0.85	13.6	[8]
		950		0.7		1030	1.1	0.78	0.78	[35]
Y_2O_3	5	976		1.7	1076	14	0.5	0.78	[35]	[15]
		977	1.2	1.99						
Y_2O_3	5	978		2.23	1032	1.42	1.42	0.97	[11]	[11]
		978		2.08		1032	1.0	0.97	0.97	
	5	978		1.15	1032	1.58	1.58	0.82	[11]	[11]
		978		2.18		1032	1.26	0.82	0.82	
	4	976			1032	1.02	0.82	0.82	[14]	[14]
		950				1074	0.41	0.82	0.82	
	6	951		0.74	1032	15	1.4	0.82	[3]	[3]
		977		2.07		1076	17	0.38	0.82	
	2.5	976			1031	0.95	0.82	0.82	[10]	[10]
		948				1076	0.50	0.82	0.82	
$\text{Lu}_{0.5}\text{Y}_{1.5}\text{O}_3$	6	950		0.71	1032	16	1.3	0.82	[3]	[3]
		976		1.70		1077	21	0.39	0.82	
$\text{Lu}_{0.5}\text{Y}_{1.5}\text{O}_3$	5	950		0.7	1030	1.1	0.76	0.76	[36]	[36]
		976		1.8		1076	0.5	0.76	0.76	
$\text{Lu}_{0.3}\text{Y}_{1.7}\text{O}_3$	5	950		0.7	1030	1.1	0.7	0.7	[36]	[36]
		976		1.7		1076	0.5	0.7	0.7	
Lu_2O_3	6	950		0.78	1034	16	1.37	0.82	[3]	[3]
		976		2.32		1079	18	0.39	0.82	
	6	976		3.2	1032	1.1	0.82	0.82	[3]	[3]
		948		1.1		1079	0.30	0.82	0.82	
Lu_2O_3	947			0.62	1033	0.84	0.84	0.82	[18]	[18]
		976		1.03		1080	0.21	0.82	0.82	
Lu_2O_3^*	6	976		2.5	1032	11.5	1.10	0.82	12.5	[8]
		976		0.44		1040	11.5	1.30	0.80	16.5
Sc_2O_3^*	3				1030	1.4	0.68	0.68	[37]	[37]
						1094	0.25	0.68	0.68	
KYW*	981		3.5	13.3	1025	16	3	0.6	3	[8]
		981	3.7	12		1023	20	2.8	0.6	3.5
$\text{Gd}_{1.4}\text{Lu}_{0.5}\text{Yb}_{0.1}\text{O}_3$	5	953		2.2	1031	1	1.07	1.07	1.07	[C]
		977		0.8		1073	0.4	1.07	1.07	

literature, where the difference between measured and real Yb^{3+} lifetime was in the range of 13–21% [32].

The main disadvantage of Yb-doped hosts is their quasi-three-level nature caused by the thermal population of the higher Stark levels of the $^2\text{F}_{7/2}$ manifold. This thermal population has deleterious effects on the radiation trapping of the emission by the thermally populated lower Stark state, which contains roughly 5% of the $^2\text{F}_{7/2}$ population at room temperature [31]. In the well-known radiation trapping effect, photons that are spontaneously emitted from the metastable level are trapped by ions in the ground state by reabsorption. These excited ions relax by spontaneously emitting more photons, which are then reabsorbed, and the entire process is repeated [33]. Therefore, the measured fluorescence lifetime is longer than the lifetime of a single Yb^{3+} ion. These reabsorption and radiation trapping phenomena ultimately limit the usefulness of the F-L method in obtaining accurate emission cross-section values, especially from highly doped bulk samples, which leads to underestimation of the stimulated emission cross-sections by as much as 30% [17]. However, the absolute value for the absorption cross section predicted by the FL relation is nearly accurate, and therefore it remains a parameter of indicative value.

Fig. 6 shows the emission cross-sections obtained using measured (green line) and calculated (red line) lifetime. The high-energy side of the emission cross-section spectra calculated by the F-L theory was affected by reabsorption phenomena which caused the lowering of the high-energy part of emission spectra, especially for $(^2\text{F}_{7/2})_0 \leftrightarrow (^2\text{F}_{5/2})_0$ transitions. The effect of reabsorption can be reduced by grinding the sample. **Fig. S4** shows the emission spectra of the powdered and bulk $\text{Gd}_{1.4}\text{Lu}_{0.5}\text{Yb}_{0.1}\text{O}_3$ samples. On the other hand, the reciprocity methods allow calculation of the emission cross-sections from corresponding absorption spectra avoiding the effect of radiation trapping [32] by the following equation:

$$\sigma_{em}(\lambda) \approx \sigma_{abs}(\lambda) \cdot \left(\frac{Z_l}{Z_u} \right) \exp \left[\frac{-\left(E_{z_l} - hc/\lambda \right)}{k_B T} \right] \quad (5)$$

where h is Planck's constant, k_B is Boltzmann's constant, T is the temperature, E_{z_l} is the net free energy required to excite one Yb^{3+} ion from the lowest Stark level of the $^2\text{F}_{7/2}$ state to the lowest Stark level of the $^2\text{F}_{5/2}$ state at temperature T , and Z_u and Z_l are partition functions.

The reciprocity method allows the emission spectrum in absolute cross-section units to be calculated from the corresponding absorption cross-section lineshape. The required information includes the ratio of the partition functions of the lower and upper states, Z_l , Z_u , and the zero-line energy E_{z_l} . Z_l and Z_u are usually obtained from the energy levels of the manifolds and the Stark levels within these manifolds. Previously, the values of Z_l/Z_u have been calculated for phosphate, germanate and silicate glasses at room temperature (0.98, 0.97 and 0.83, respectively) [32]. While these data are not available for Yb-doped sesquioxides, the value of Z_l/Z_u (1) was used for calculations. Within this approximation, the total uncertainty in the σ_{em} value was 15%. The calculated emission cross-section for $\text{Gd}_{1.4}\text{Lu}_{0.5}\text{Yb}_{0.1}\text{O}_3$ ceramics is shown in **Fig. 6** (black line). The lineshape of the emission cross-section obtained corresponds well with that reported in the literature for other Yb-doped materials, while the strongest emission peak was found at 980 nm [32].

An attractive aspect of McCumber's theory is that its validity is based on very general assumptions. One assumption, which is widely recognized, is that there is a thermal distribution of population among the individual Stark components of each Stark manifold. Another assumption, not as widely recognized, is that it is strictly valid only when the linewidth of each individual transition between Stark levels is less than $k_B T$ [34]. At room temperature this seems to be a fairly good approximation for the $(^2\text{F}_{7/2})_0 \leftrightarrow (^2\text{F}_{5/2})_0$ transitions, since typical homogeneous and inhomogeneous components of linewidth are in the range up to 35 cm^{-1} compared with $k_B T \sim 200 \text{ cm}^{-1}$. However, the transition between

$(^2\text{F}_{5/2})_{1,2}$ and $(^2\text{F}_{7/2})_{1,2,3}$ Stark level is comparable with $k_B T$ at room temperature. Because these transitions are so strongly overlapped, it was difficult to define the spectral linewidth, and the estimated values of the spectral linewidths were in the range of 50–170 cm^{-1} . Therefore, the McCumber transform introduces a distortion in the emission cross-sections calculated in which the low-energy side of the spectrum is increased, and the high-energy side is decreased [34].

The reciprocity and F-L methods of predicting the emission cross-sections is largely inaccurate (i.e., by up to 30%). Combination of these two methods allows the exclusion of the uncertainty in the determination of emission cross-sections in the high-energy region for the F-L method caused by reabsorption and uncertainty in the low-energy region for the reciprocity method caused by high spectral linewidth for transitions between Stark levels. The stimulated-emission cross-section for $\text{Gd}_{1.4}\text{Lu}_{0.5}\text{Yb}_{0.1}\text{O}_3$ ceramics was $9.7 \cdot 10^{-21} \text{ cm}^2$ (reciprocity) and $8.4 \cdot 10^{-21} \text{ cm}^2$ (F-L) at 1031 nm and $3.7 \cdot 10^{-21} \text{ cm}^2$ (reciprocity) and $3.9 \cdot 10^{-21} \text{ cm}^2$ (F-L) at 1073 nm. The calculated values were close to the estimated values of the emission cross-section for other Yb-doped sesquioxides (**Table 2**). The gain cross-section can be calculated using absorption and emission cross-sections according to the following equation:

$$\sigma_G(\lambda) = P \times \sigma_{em}(\lambda) - (1 - P) \times \sigma_{abs}(\lambda) \quad (9)$$

where P is the population inversion ratio, $P = N_u/N_0$, N_u and N_0 are the number of Yb^{3+} ions at the lasing $^2\text{F}_{5/2}$ level and the total number of Yb^{3+} ions, respectively [9].

Fig. 7 shows the set of gain cross-section spectra for several P values from 0 to 1. According to the data obtained, the positive gain cross-section at 1030 nm and 1072 nm can be achieved when the inversion ratio P is 0.1 or higher. Therefore, the low inversion ratio indicates a low pumping threshold for $\sim 1 \mu\text{m}$ laser operation of $\text{Gd}_{1.4}\text{Lu}_{0.5}\text{Yb}_{0.1}\text{O}_3$ ceramics.

4. Conclusion

$\text{Gd}_{1.4}\text{Lu}_{0.5}\text{Yb}_{0.1}\text{O}_3$ ceramics with good optical transparency were successfully fabricated by hot pressing of nanopowders using lithium fluoride as a sintering additive. The X-ray diffraction results show the presence of two phases. The first with a cubic structure similar to those of pure Lu_2O_3 and Gd_2O_3 , and the second with a monoclinic structure $(\text{Lu},\text{Gd})_2\text{O}_3$. The reflection peaks of the monoclinic phase were broadened, which indicates lack of completion of the phase transition from

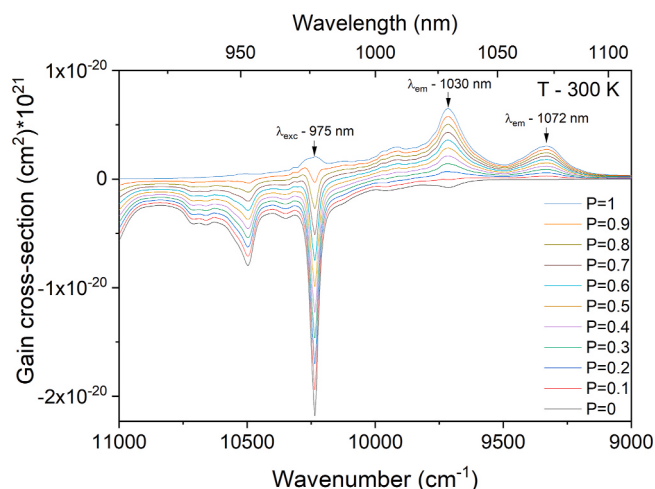


Fig. 7. The calculated gain cross-section of $\text{Gd}_{1.4}\text{Lu}_{0.5}\text{Yb}_{0.1}\text{O}_3$ ceramics from emission cross-section calculated by Fuchtbauer-Ladenburg equation (red line on **Fig. 2**). (For interpretation of the references to colour in this figure legend, the reader is referred to the Web version of this article.)

the monoclinic to the cubic phase. It should be noted that the SEM analysis revealed no secondary phases in our samples. The elemental mapping shows homogeneous distribution of the Gd, Lu, Yb and O elements within the sample.

The absorption and emission spectra as well as decay curves were measured at room temperature. In-line transmission at 500, 1100 and 2500 nm was 54%, 71%, and 76%, respectively. The absorption coefficients of Gd^{3+} ions at 275 nm and 315 nm were 48.5 cm^{-1} and 10.5 cm^{-1} , respectively. The absorption coefficient at 975 nm was 28.4 cm^{-1} and the absorption cross-section was $2.18 \cdot 10^{-20} \text{ cm}^2$. The Yb^{3+} emission bands were in the range of 900–1150 nm with maximums of 975 nm, 1008 nm, 1030 nm, and 1072 nm. The measured luminescence lifetime of the ${}^2\text{F}_{5/2}$ state of Yb^{3+} ions in the $\text{Gd}_{1.4}\text{Lu}_{0.5}\text{Yb}_{0.1}\text{O}_3$ ceramic sample was found to be 1.07(1) ms.

Two different approaches were used to calculate the emission cross-sections, namely: (i) the reciprocity method (McCumber method), and (ii) the Fuchtbauer-Ladenburg (F-L) equation. The reciprocity and F-L methods' prediction of the emission cross-section was largely inaccurate (i.e., by up to 30%). The stimulated-emission cross-section for $\text{Gd}_{1.4}\text{Lu}_{0.5}\text{Yb}_{0.1}\text{O}_3$ ceramics was $9.7 \cdot 10^{-21} \text{ cm}^2$ (reciprocity) and $8.4 \cdot 10^{-21} \text{ cm}^2$ (F-L) at 1031 nm and $3.7 \cdot 10^{-21} \text{ cm}^2$ (reciprocity) and $3.9 \cdot 10^{-21} \text{ cm}^2$ (F-L) at 1073 nm. The values calculated were close to the estimated values of emission cross-sections for other Yb-doped sesquioxides. According to the data obtained, a positive gain cross-section at 1030 nm and 1072 nm can be achieved when the inversion ratio P is 0.1 or higher. All the results show that $\text{Gd}_{1.4}\text{Lu}_{0.5}\text{Yb}_{0.1}\text{O}_3$ transparent ceramics can be used as a potential active medium for mid-infrared high-power lasers.

CRediT authorship contribution statement

Mykhailo Chaika: Conceptualization, Investigation, Project administration, Resources, Supervision, Writing – original draft. **Stanislav Balabanov:** Investigation, Resources, Writing – review & editing. **Dmitry Permin:** Investigation.

Declaration of competing interest

The authors declare that they have no known competing financial interests or personal relationships that could have appeared to influence the work reported in this paper.

Acknowledgement

This work was supported by the Ministry of Science and Higher Education of the Russian Federation by the State Task executed in the IChHPS RAS, Project No. FFRN-2019-005.

Appendix A. Supplementary data

Supplementary data to this article can be found online at <https://doi.org/10.1016/j.omx.2021.100123>.

References

- [1] M. Chaika, O. Vovk, G. Mancardi, R. Tomala, W. Strek, Dynamics of Yb^{2+} to Yb^{3+} ion valence transformations in $\text{Yb}: \text{YAG}$ ceramics used for high-power lasers, Opt. Mater. 101 (2020) 109774, <https://doi.org/10.1016/j.optmat.2020.109774>.
- [2] O.V. Palashov, A.V. Starobor, E.A. Perevezentsev, I.L. Snetkov, E.A. Mironov, A. I. Yakovlev, S.S. Balabanov, D.A. Permin, A.V. Belyaev, Thermo-optical studies of laser ceramics, Materials 14 (2021) 3944, <https://doi.org/10.3390/ma14143944>.
- [3] R.N. Maksimov, A.S. Yurovskikh, V.A. Shitov, Fabrication, microstructure, and spectroscopic properties of transparent Yb 0.118 Lu 0.464 Y 1.418 O 3 ceramics, Phys. Status Solidi 217 (2020) 1900883, <https://doi.org/10.1002/pssa.201900883>.
- [4] P. Klopp, New Yb 3+ -doped laser materials and their application in continuous-wave and mode-locked lasers, Humboldt-Universität zu Berlin, Mathematisch-Naturwissenschaftliche Fakultät I, 2006, <https://doi.org/10.18452/15548>.
- [5] M. Chaika, R. Tomala, W. Strek, Laser induced broadband Vis and NIR emission from $\text{Yb}: \text{YAG}$ nanopowders, J. Alloys Compd. 865 (2021), <https://doi.org/10.1016/j.jallcom.2021.158957>.
- [6] X.-X. Wu, M. Cheng, Estimations of the electron-phonon coupling parameters of the spectral lines in GaAs: Er3+ and $\text{Y}_3\text{Al}_5\text{O}_12:\text{Yb}^{3+}$, Optik 243 (2021) 167423, <https://doi.org/10.1016/j.jlelo.2021.167423>.
- [7] M. Chaika, S. Balabanov, D. Permin, Optical spectra and gain properties of Er3+: Lu_2O_3 ceramics for eye-safe 1.5-μm lasers, Opt. Mater. 112 (2021) 110785, <https://doi.org/10.1016/j.optmat.2020.110785>.
- [8] M. Maruyama, H. Okada, Y. Ochi, K. Nagashima, Sub-picosecond regenerative amplifier of Yb-doped Y_2O_3 ceramic thin disk, Opt Express 24 (2016) 1685, <https://doi.org/10.1364/OE.24.001685>.
- [9] M.A.A. Chaika, N.A.A. Dulina, A.G.G. Doroshenko, S.V.V. Parkhomenko, O.V. V. Gayduk, R. Tomala, W. Strek, D. Hreniak, G. Mancardi, O.M.M. Vovk, Influence of calcium concentration on formation of tetravalent chromium doped $\text{Y}_3\text{Al}_5\text{O}_12$ ceramics, Ceram. Int. 44 (2018) 13513–13519, <https://doi.org/10.1016/j.ceramint.2018.04.182>.
- [10] J. Kong, D.Y. Tang, J. Lu, K. Ueda, Spectral characteristics of a Yb-doped Y_2O_3 ceramic laser, Appl. Phys. B 79 (2004) 449–455, <https://doi.org/10.1007/s00340-004-1594-3>.
- [11] G. Stanciu, F. Voicu, C.-A. Brandus, C.-E. Tihon, S. Hau, C. Gheorghe, G. Croitoru, L. Gheorghe, M. Dumitru, Enhancement of the laser emission efficiency of $\text{Yb}: \text{Y}_2\text{O}_3$ ceramics via multi-step sintering method fabrication, Opt. Mater. 109 (2020) 110411, <https://doi.org/10.1016/j.optmat.2020.110411>.
- [12] M. Chaika, W. Paszkowicz, W. Strek, D. Hreniak, R. Tomala, N. Safranova, A. Doroshenko, S. Parkhomenko, P. Dluzewski, M. Kozłowski, O. Vovk, Influence of Cr doping on the phase composition of $\text{Cr}, \text{Ca}: \text{YAG}$ ceramics by solid state reaction sintering, J. Am. Ceram. Soc. 102 (2019) 2104–2115, <https://doi.org/10.1111/jace.16024>.
- [13] M.A. Chaika, P. Dluzewski, K. Morawiec, A. Szczepanska, K. Jabłonska, G. Mancardi, R. Tomala, D. Hreniak, W. Strek, N.A. Safranova, A.G. Doroshenko, S. V. Parkhomenko, O.M. Vovk, The role of Ca^{2+} ions in the formation of high optical quality $\text{Cr}^{4+}, \text{Ca}: \text{YAG}$ ceramics, J. Eur. Ceram. Soc. 39 (2019) 3344–3352, <https://doi.org/10.1016/j.jeurceramsoc.2019.04.037>.
- [14] A. Shirakawa, K. Takaichi, H. Yagi, J. Bisson, J. Lu, M. Musha, K. Ueda, T. Yanagitani, T. Petrov, A. Kaminskii, Diode-pumped mode-locked $\text{Yb}^{3+}: \text{Y}_2\text{O}_3$ ceramic laser, Opt Express 11 (2003) 2911, <https://doi.org/10.1364/OE.11.002911>.
- [15] S. Balabanov, D. Permin, T. Evstropov, P. Andreev, L. Basyrova, P. Camy, M. Baranov, X. Mateos, P. Loiko, Hot pressing of $\text{Yb}: \text{Y}_2\text{O}_3$ laser ceramics with LiF sintering aid, Opt. Mater. 119 (2021) 111349, <https://doi.org/10.1016/j.optmat.2021.111349>.
- [16] D.A. Permin, S.S. Balabanov, I.L. Snetkov, O.V. Palashov, A.V. Novikova, O. N. Klyusik, I.V. Ladenkov, Hot pressing of $\text{Yb}: \text{Sc}_2\text{O}_3$ laser ceramics with LiF sintering aid, Opt. Mater. 100 (2020) 109701, <https://doi.org/10.1016/j.optmat.2020.109701>.
- [17] L.S. Qin, Y.T. Wu, H.S. Shi, W.X. Chai, K.Y. Shu, G.H. Ren, X.F. Chen, Effects of doping Lu_2O_3 into Gd_2O_3 on phase transformation and luminescence, IEEE Trans. Nucl. Sci. 56 (2009) 2979–2982, <https://doi.org/10.1109/TNS.2009.2026649>.
- [18] Z. Liu, G. Toci, A. Pirri, B. Patrizi, Y. Feng, J. Wei, F. Wu, Z. Yang, M. Vannini, J. Li, Fabrication, microstructures, and optical properties of $\text{Yb}: \text{Lu}_2\text{O}_3$ laser ceramics from co-precipitated nano-powders, J. Adv. Ceram. 9 (2020) 674–682, <https://doi.org/10.1007/s04150-020-0403-8>.
- [19] Q. Liu, J. Li, J. Dai, Z. Hu, C. Chen, X. Chen, Y. Feng, J. Li, Fabrication, microstructure and spectroscopic properties of $\text{Yb}: \text{Lu}_2\text{O}_3$ transparent ceramics from co-precipitated nanopowders, Ceram. Int. 44 (2018) 11635–11643, <https://doi.org/10.1016/j.ceramint.2018.03.238>.
- [20] X. Liu, W. Jing, Q. Hao, D. Li, J. Guo, J. Liu, Q. Peng, Characterisation of passively Q-switched $\text{Yb}: \text{Lu}_2\text{O}_3$ ceramic laser based on graphdyne absorber, Infrared Phys. Technol. 115 (2021) 103739, <https://doi.org/10.1016/j.infrared.2021.103739>.
- [21] L. Basyrova, P. Loiko, R. Maksimov, V. Shitov, J.M. Serres, U. Griebner, V. Petrov, M. Aguiló, F. Díaz, X. Mateos, Comparative study of $\text{Yb}: \text{Lu}_3\text{Al}_5\text{O}_12$ and $\text{Yb}: \text{Lu}_2\text{O}_3$ laser ceramics produced from laser-ablated nanopowders, Ceram. Int. 47 (2021) 6633–6642, <https://doi.org/10.1016/j.ceramint.2020.10.253>.
- [22] R.N. Maksimov, V.A. Shitov, V.V. Platonov, A.S. Yurovskikh, G. Toci, B. Patrizi, M. Vannini, A. Pirri, Hot isostatic pressing of transparent Yb^{3+} -doped Lu_2O_3 ceramics for laser applications, Ceram. Int. 47 (2021) 5168–5176, <https://doi.org/10.1016/j.ceramint.2020.10.094>.
- [23] F. Ashrafi, H. Mokhtari, S.J. Hashemifar, A. Alhaji, A combined experimental and theoretical optimization of the refractive index of $\text{Ni}_x\text{Mg}_{1-x}\text{O}$ solid solution for transparent nanocomposite applications, Ceram. Int. 46 (2020) 20061–20067, <https://doi.org/10.1016/j.ceramint.2020.05.080>.
- [24] O. Medenbach, D. Dettmar, R.D. Shannon, R.X. Fischer, W.M. Yen, Refractive index and optical dispersion of rare earth oxides using a small-prism technique, J. Opt. A Pure Appl. Opt. 3 (2001) 174–177, <https://doi.org/10.1088/1464-4258/3/3/303>.
- [25] Y.A. Kuznetsova, A.F. Zatsepin, Optical properties and energy parameters of Gd_2O_3 and $\text{Gd}_2\text{O}_3:\text{Er}$ nanoparticles, J. Phys. Conf. Ser. 917 (2017), 062001, <https://doi.org/10.1088/1742-6596/917/6/062001>.
- [26] D.C. Brown, Z. Fleischman, L.D. Merkle, L.D. Sanjeewa, C.D. McMillen, J.W. Kolis, $\text{Yb}: \text{Lu}_2\text{O}_3$ hydrothermally grown single-crystal high-resolution absorption spectra obtained between 8 and 300 K, Appl. Phys. B 126 (2020) 62, <https://doi.org/10.1007/s00340-020-7412-8>.
- [27] W.F. Krupke, Ytterbium solid-state lasers. The first decade, IEEE J. Sel. Top. Quant. Electron. 6 (2000) 1287–1296, <https://doi.org/10.1109/2944.902180>.

- [28] S.A. Payne, L.L. Chase, L.K. Smith, W.L. Kway, W.F. Krupke, Infrared cross-section measurements for crystals doped with Er³⁺, Tm³⁺, and Ho³⁺, IEEE J. Quant. Electron. 28 (1992) 2619–2630, <https://doi.org/10.1109/3.161321>.
- [29] M. Tokurakawa, K. Takaichi, A. Shirakawa, K. Ueda, H. Yagi, S. Hosokawa, T. Yanagitani, A.A. Kaminskii, Diode-pumped mode-locked Yb³⁺:Lu₂O₃ ceramic laser, Opt Express 14 (2006) 12832, <https://doi.org/10.1364/OE.14.012832>.
- [30] A.S. Pinheiro, A.M. Freitas, G.H. Silva, M.J.V. Bell, V. Anjos, A.P. Carmo, N. O. Dantas, Laser performance parameters of Yb³⁺ doped UV-transparent phosphate glasses, Chem. Phys. Lett. 592 (2014) 164–169, <https://doi.org/10.1016/j.cplett.2013.12.022>.
- [31] J. Dong, M. Bass, Y. Mao, P. Deng, F. Gan, Dependence of the Yb³⁺ emission cross section and lifetime on temperature and concentration in yttrium aluminum garnet, J. Opt. Soc. Am. B 20 (2003), <https://doi.org/10.1364/JOSAB.20.001975>, 1975.
- [32] H. Yin, P. Deng, J. Zhang, F. Gan, Determination of emission cross section of Yb³⁺ in glasses by the reciprocity method, Mater. Lett. 30 (1997) 29–33, [https://doi.org/10.1016/S0167-577X\(96\)00166-8](https://doi.org/10.1016/S0167-577X(96)00166-8).
- [33] D.S. Sumida, T.Y. Fan, Effect of radiation trapping on fluorescence lifetime and emission cross section measurements in solid-state laser media, Opt. Lett. 19 (1994) 1343, <https://doi.org/10.1364/OL.19.001343>.
- [34] R.S. Quimby, Range of validity of McCumber theory in relating absorption and emission cross sections, J. Appl. Phys. 92 (2002) 180–187, <https://doi.org/10.1063/1.1485112>.
- [35] G. Toci, A. Pirri, B. Patrizi, R.N. Maksimov, V.V. Osipov, V.A. Shitov, M. Vannini, Yb^{3+:(LuxY1-x)2O3 mixed sesquioxide ceramics for laser applications. Part II: laser performances, J. Alloys Compd. 853 (2021) 156943, <https://doi.org/10.1016/j.jallcom.2020.156943>.}
- [36] A. Pirri, G. Toci, B. Patrizi, R.N. Maksimov, V.V. Osipov, V.A. Shitov, A. S. Yurovskikh, E.V. Tikhonov, M. Becucci, M. Vannini, Yb^{3+:(LuxY1-x)2O3 mixed sesquioxide ceramics for laser applications. Part I: fabrication, microstructure and spectroscopy, J. Alloys Compd. 869 (2021) 159227, <https://doi.org/10.1016/j.jallcom.2021.159227>.}
- [37] G. Toci, J. Hostaša, B. Patrizi, V. Biasini, A. Pirri, A. Piancastelli, M. Vannini, Fabrication and laser performances of Yb:Sc₂O₃ transparent ceramics from different combination of vacuum sintering and hot isostatic pressing conditions, J. Eur. Ceram. Soc. 40 (2020) 881–886, <https://doi.org/10.1016/j.jeurceramsoc.2019.10.059>.